DOI: 10.21062/mft.2025.044 http://www.journalmt.com

Analysis of the Influence of Preparation Technology on the Structure and Properties of the CuZn10 Alloy

Anna Knaislová (0000-0002-3508-9725)[1,2], Jakub Kabrle (0009-0007-6165-6387)[1]
[1]Faculty of Mechanical Engineering, J. E. Purkyne University in Usti nad Labem. Pasteurova 3334/7, 400 01 Usti nad Labem. Czech Republic. E-mail: anna.knaislova@ujep.cz, kuba.kabrle@email.cz
[2]Faculty of Environment, J. E. Purkyne University in Usti nad Labem. Pasteurova 3632/15, 400 96 Ústí nad Labem, Czech Republic

The CuZn10 alloy, a prominent brass variant known for its excellent cold formability, corrosion resistance, and suitability for various cold forming processes such as bending and stamping, finds widespread application across numerous industries. Optimizing its performance for specific industrial demands necessitates a thorough understanding of how different preparation technologies influence its intrinsic properties. This study provides a comprehensive examination into the impact of various processing routes on both the structural evolution and mechanical characteristics of deep-drawing CuZn10 brass. Utilizing advanced analytical techniques, including Electron Backscatter Diffraction (EBSD) analysis, the research systematically investigates microstructural changes, grain orientation, and texture development resulting from distinct manufacturing processes. The findings delineate clear correlations between specific preparation methodologies and the resulting mechanical properties, such as hardness, strength, and ductility. This work aims to establish a foundational understanding that can guide industrial practitioners in selecting optimal processing technologies to tailor CuZn10 alloy for enhanced performance and efficiency in its diverse applications. The insights gained are critical for refining manufacturing protocols and improving material quality in an industrial context.

Keywords: Brass, CuZn10, Electron backscatter diffraction analysis, Casting, Rolling

1 Introduction

CuZn10 is a copper alloy containing 10% zinc (brass) and is one of the strengthened copper alloys. CuZn10 has very good cold formability and is suitable for bending, stamping and other cold forming processes. The alloy can be soldered or welded. As the zinc content increases, strength increases, but conductivity and ductility decrease. CuZn10 has good corrosion resistence, high hardness, strength and duktility, which is used in many industry sectors, such as automotive, energy and military industry [1-3].

This alloy can be processed using several technologies. The copper alloy is first melted in an electric crucible furnace at a temperature of 1,050 °C. After the copper has melted, the required amount of zinc is added to the alloy, in this case around 10%. A very small amount of additional zinc may then be added to the brass alloy to compensate for the evaporation of zinc during the melting process. The molten metal is poured into a mold, which can be made of various materials such as sand and is designed to create the desired shape of the final casting. In this prepared mold, the molten metal then solidifies and becomes an ingot [4,5]. The introduction of a modern production process in the field of continuous casting allows to have a brass ingot that is highly homogeneous and has a top quality that guarantees higher customer satisfaction. Castings can be obtained by using casting technologies that include, for example, pressure casting, gravity casting and continuous casting [6].

The initial heterogeneous structure, in which defects such as voids, porosity, segregation can often occur, is formed by large columnar grains. These grains must be changed by a hot rolling process that breaks the grain boundaries and forms new grains with stronger grain boundaries and a uniform material structure [7, 8]. Hot rolling of the CuZn10 alloy must be carried out by heating the alloy above the recrystallization temperature and then deforming it in rolls to the desired shape. The ingots are heated above the desired recrystallization temperature in a furnace. These hot ingots are then passed over steel rolls, the surface of which can be cooled with running water to reduce the thickness of the brass. During this operation, the overall length of the brass is also increased [9]. After cooling, the brass is then passed through a milling machine also known as a Scalper. This machine removes the outer coating of brass, which can be tarnished due to oxides formed when the metal is exposed to air.

Cold rolling is performed on a metal below its recrystallization temperature (usually at room temperature), which increases the strength by strain hardening by up to 20%. Common cold-rolled products are

ISSN 1213–2489
e-ISSN 2787–9402

sheets, strips and bars. These products can usually be rolled to much thinner thicknesses than would be possible with hot-rolling [10-12]. If hot-rolled brass begins to solidify, it loses its ductility, and therefore must be heated to a certain temperature before further rolling, at which it becomes more ductile again. This process is called annealing. For the CuZn10 alloy, the first annealing time is 10 minutes at a temperature of 650 °C, followed by a second annealing time of 7 hours and a temperature of 450 °C, based on a study by Yilmaz S. In general, the CuZn10 alloy can be annealed in the temperature range of 450 to 680 °C [13-16].

Larger pieces of hot-rolled brass can be placed in a sealed furnace and annealed together. Smaller pieces can be placed on a conveyor belt and fed continuously through the furnace with an airtight closure at each end.

In both methods, the atmosphere inside the furnace is a neutral gas such as nitrogen to prevent the brass from reacting with oxygen and forming undesirable oxides on its surface [17].

The annealed pieces of brass are then passed through another set of rolls to further reduce their thickness. This process is called cold rolling. Cold rolling deforms the internal structure of the brass at the grain level and increases its strength and hardness. The more the thickness is reduced, the stronger and harder the material becomes. In some operations, the pieces of brass are joined together into one long continuous sheet and passed through a series of annealing furnaces and rolls arranged in series. At this point, the wide sheets can be cut into narrower sections to produce a brass strip. The strip can then be subjected to an acid bath and rinsed to clean it [18].

Deep drawing of brass is a complex process that requires the design and preparation of a die. The process involves stretching the blanks and then transferring them to a die that is to be cut into the desired shape. Deep drawing of brass is used in many industries, including cartridge case manufacturing, musical instruments, and plumbing applications. When preparing for deep drawing of brass, several factors must be considered, such as the thickness of the brass, the shape and size of the blank, the shape of the final product, the speed of the press, the radius, the draw ratio, the plastic deformation ratio, the surface finish of the die, the temperature of the die, and the lubricant. The thickness of the brass blanks depends on the desired size and strength of the final product. Thicker brass blanks are inherently stiffer than thinner brass blanks—this allows the thicker blanks to hold together better during the deep drawing process. Excessive friction can also disrupt the deep drawing process. If the friction during the process is too large, uneven forming or breakage is likely to occur. To prevent this, it is necessary to select the right type of lubricant. The draw ratio is one of the most important factors to consider when deep drawing CuZn10 brass. This ratio is defined as the difference between the draw bar and the size of the blank [19-21].

2 Experimental

Four strips were received from Povrly Copper Industries a.s., each prepared using a different technology. The first sample was a cast strip only (Fig. 1), the second was a hot-rolled sample (Fig. 2), the third sample was processed by cold rolling (Fig. 3), and the fourth sample was processed by cold rolling twice and then annealed at 500 °C for 1 hour, thus also investigating the effect of annealing on the microstructure and hardness of the alloy.

Fig. 1 *Sample prepared by casting*

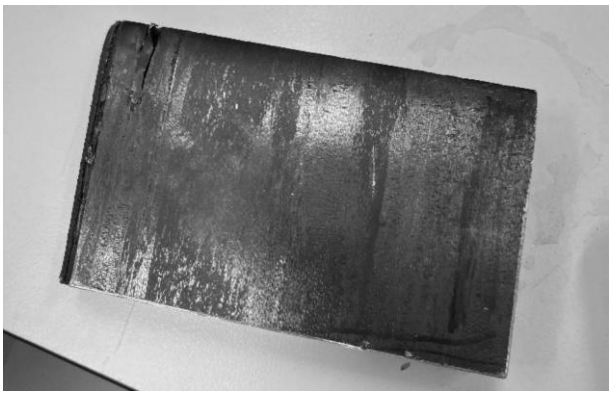

Fig. 2 *Sample prepared by hot-rolling*

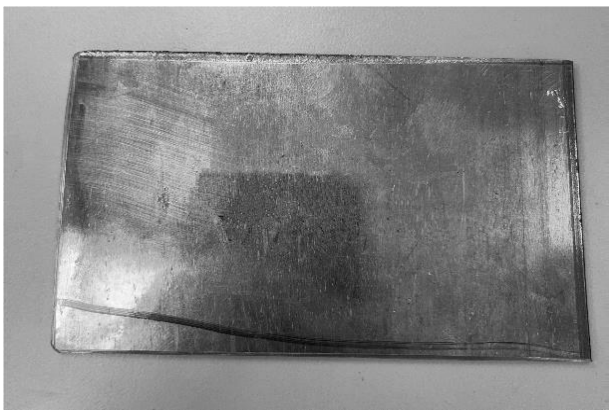

Fig. 3 *Sample prepared by cold-rolling*

indexed on http://www.webofscience.com and http://www.scopus.com

The samples were cut on a Struers Lobotom-5 metallographic saw and a Struers Secotom-20 automatic cutting saw. After cutting, the samples were embedded with a mixture of blue acrylic powder medium VariDur. The embedded samples were then ground on a Saphir 360 polisher. A series of grinding wheels with different grits, specifically from P80 to P4000, were used for this process. After grinding was completed, each sample was polished on polishing wheels, with two different diamond polycrystalline polishing suspensions (particle sizes 3 and 1 μm) being applied in turn.

Polishing and etching were performed on a fully automatic KrisTall 620 polisher. This equipment uses electrolytic processes with prescribed electric current and voltage. 50% phosphoric acid was chosen as the etching medium. The conditions of electrolytic polishing and etching were chosen according to previous experience with polishing and etching of brass and the voltage and current values used for individual samples are shown in Table 1. Polishing and etching were always performed for 30 seconds.

Tab. 1 *Values of electric currents and voltages during etching and polishing*

	Voltage [V]	Current [A]	
Casting	1.5	2.6	Polishing
	1.5	0.44	Etching
Hot-rolling	1.5	3.0	Polishing
	1.5	0.48	Etching
Cold-rolling	1.5	3.5	Polishing
	1.5	0.3	Etching
Cold-rolling + annealing	1.5	3.4	Polishing
	1.5	0.42	Etching

After polishing and etching, the samples were observed using an Olympus LEXT OLS 5100 laser confocal microscope. For a more detailed investigation of the microstructure of the samples, a Tescan Vega 3 XMU scanning electron microscope was selected.

The electron backscatter diffraction (EBSD) method was selected on the scanning electron microscope to determine the grain size and their orientation. The copper indexing (cubic structure) was selected, the parameters of this phase are given in Tab. 2. All samples were placed at an angle of 70 °C to the detector (they were glued to a special holder) to be able to observe the Kikuchi lines emerging from the sample surface on a fluorescent phosphor screen. The acceleration voltage was 30 kV at a working distance of 15 mm, binning (matrix) 4x4 (in the case of rolled samples 2x2). The orientation of the samples is shown in Fig. 4. For all samples, maps of inverse pole figures in the direction of all three axes with the appropriate color keys, maps of dislocation density, grain boundaries including twinning, and average grain size were measured.

Tab. 2 *Parameters of indexed copper*

Phase	a	b	c	Alpha	Beta	Gamma	Space group	Database
Copper	3.61Å	3.61Å	3.61Å	90.00°	90.00°	90.00°	225	HKL

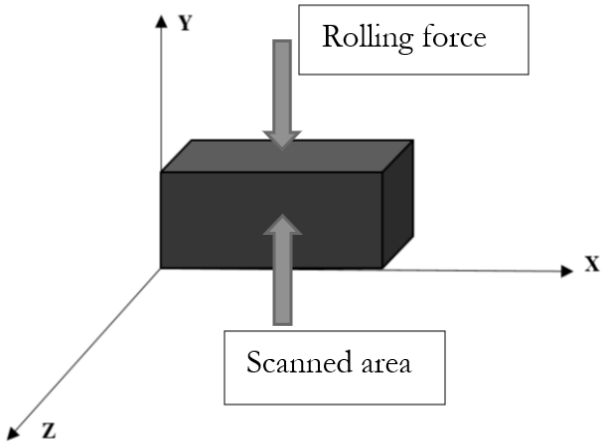

Fig. 4 *Orientation and coordinate system of sample axes for EBSD*

3 Results and discussion

3.1 Microstructure of the samples

First, the samples were observed on an Olympus LEXT OLS 5100 laser confocal microscope in order to observe the largest possible area. The microstructure of the sample after casting is shown in Fig. 5. The figure shows that the microstructure consists of large grains, which are not visible in their entirety even at the lowest magnification of the microscope. For this reason, it is not possible to describe the grain boundaries and grain size.

After hot rolling (see Fig. 6) the etched structure is more pronounced and the individual grains are better visible. The individual grain boundaries, including twinning, are also very pronounced in the picture.

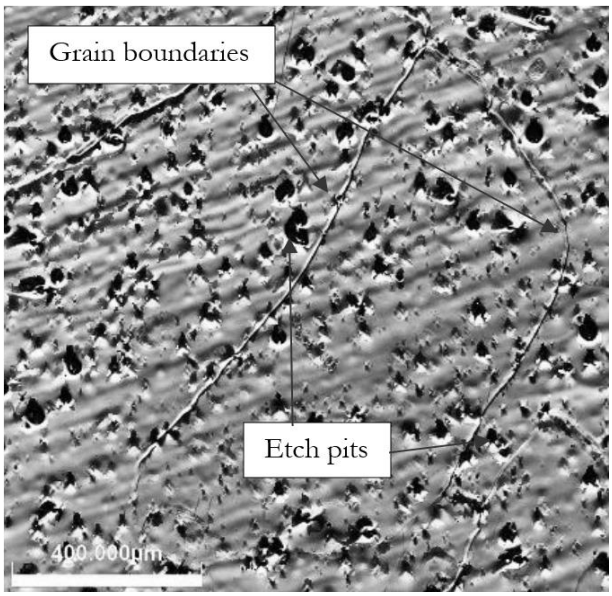

Fig. 5 *Microstructure of the sample after casting*

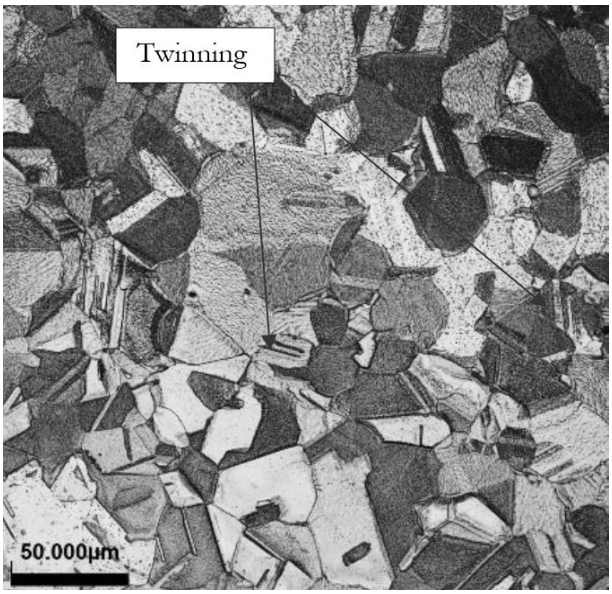

Fig. 6 *Microstructure of the sample after hot-rolling*

During the cold rolling process, the individual grains of the material are stretched in the direction in which the rolling is carried out. This process causes the grains in the material to undergo significant deformation. As a result of this deformation, the grain boundaries become less visible (see Fig. 7). During the cold rolling, the stretched grains in the rolling direction are again visible. In addition, there is also a strongly deformed structure. This structural deformation is caused by the deformation of the CuZn10 lattice.

The sample that underwent the annealing process should exhibit clearly visible grain boundaries; however, as shown in Fig. 8, the grain boundaries are less distinct, with only faint traces visible. This was caused by insufficient sample preparation prior to measurement.

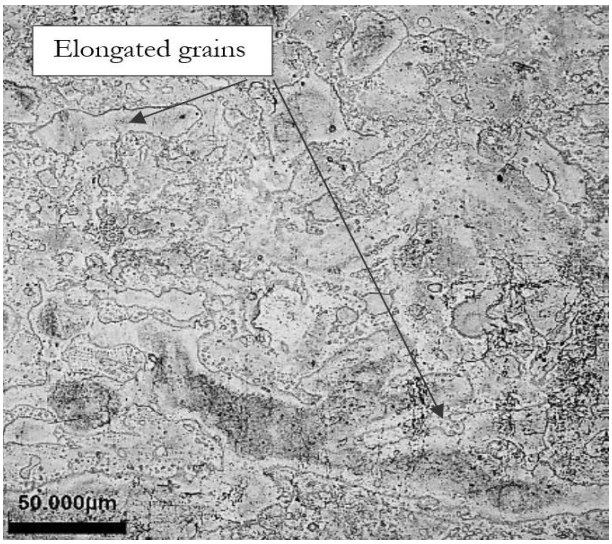

Fig. 7 *Microstructure of the sample after cold-rolling*

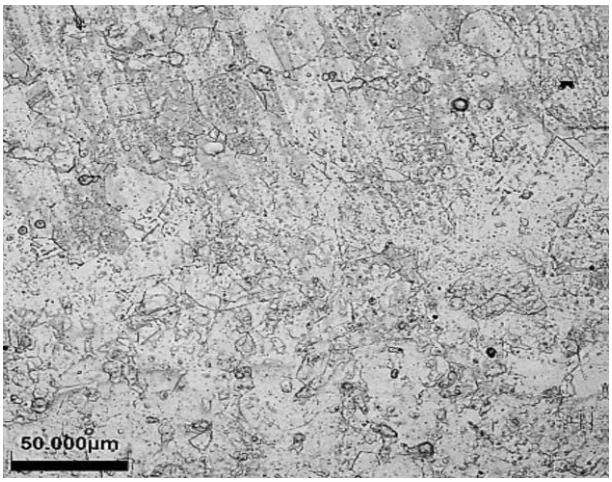

Fig. 8 *Microstructure of the sample after cold-rolling + annealing*

3.2 EBSD analysis

Fig. 9 shows the sample after casting with the area selected for EBSD analysis. Figures 10, 11 and 12 show the inverse pole figure maps in the direction of the individual axes for this sample. Since the grains are huge and cannot be included in one image, the following information may be inaccurate. The individual grains are randomly oriented with a preferential direction in the <111> direction parallel to the x-axis. This is confirmed by Figure 13. The grain boundaries were divided into low-angle (5–15°) and high-angle (above 15°). The selected area of the sample contains most of the high-angle grain boundaries (see Figure 14) and no twinning, which occurs in the <111> direction in the fcc structure. A GND Density map was also created in combination with a grain boundary map (see Fig. 15) to investigate the dislocation concentration. The dislocation density in the selected area of the sample ranges from values close to zero (places marked in dark blue in Fig. 15) to values of approximately $1.5 \cdot 10^{14}/m^2$ (places in light green).

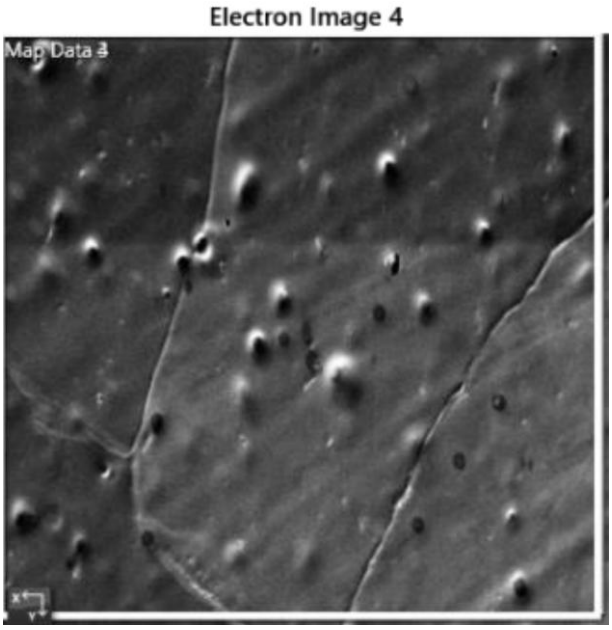

Fig. 9 *Sample area selected for EBSD analysis (sample after casting)*

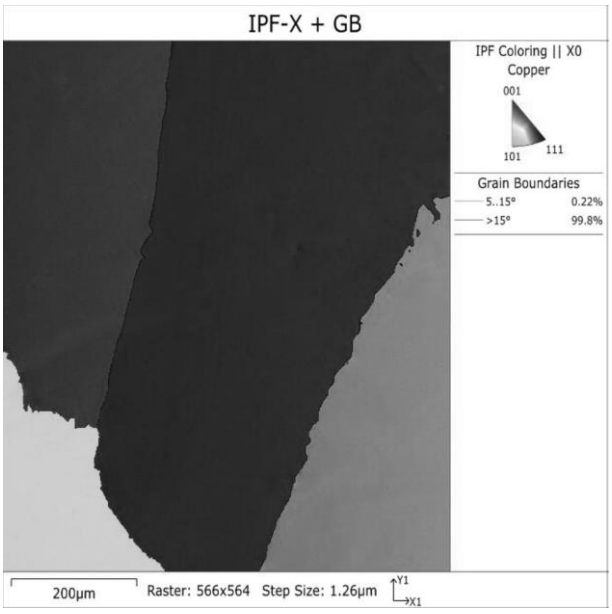

Fig. 10 *Inverse pole figure map, axis x (sample after casting)*

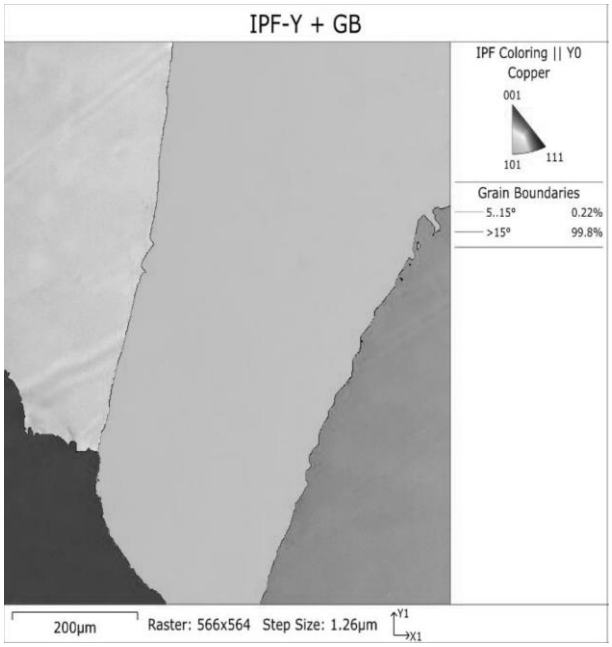

Fig. 11 *Inverse pole figure map, axis y (sample after casting)*

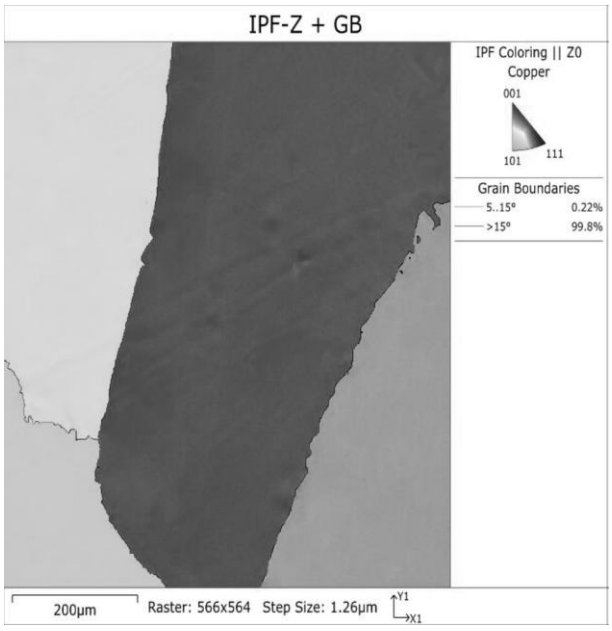

Fig. 12 *Inverse pole figure map, axis z (sample after casting)*

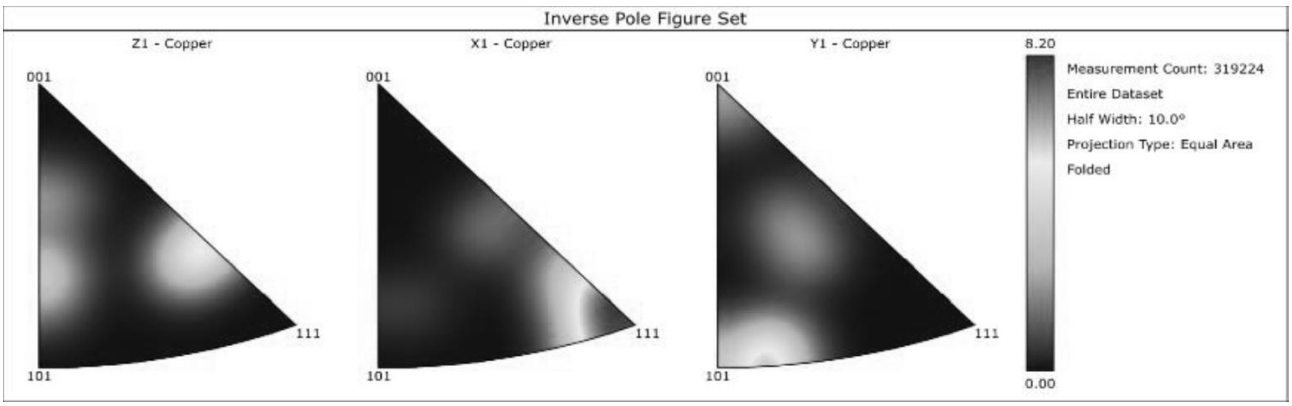

Fig. 13 *Inverse pole images for all three axes for the sample after casting*

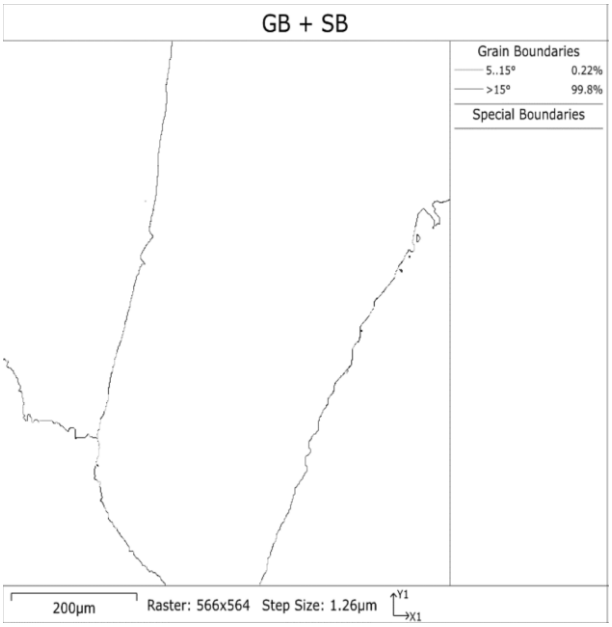

Fig. 14 *Grain boundaries including twinning in the sample after casting*

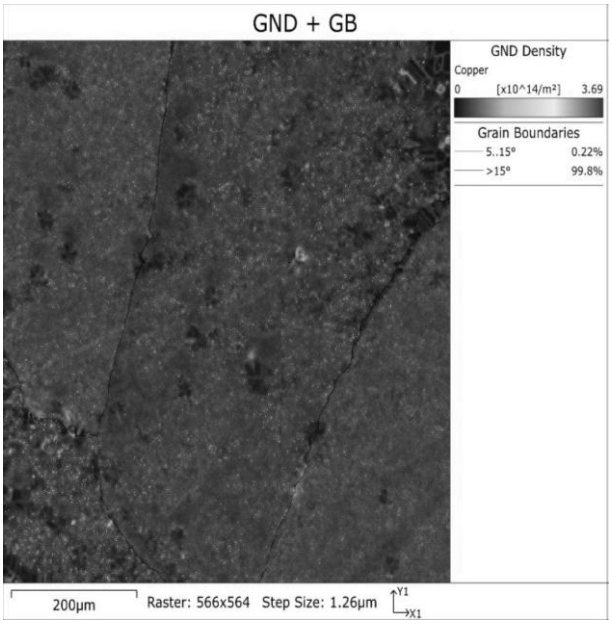

Fig. 15 *GND density of the sample after casting*

Figure 16 shows the sample after hot-rolling with the area selected for EBSD analysis. Figures 17, 18 and 19 show the inverse pole figure maps in the direction of the individual axes for the sample after hot-rolling. The individual grains are randomly oriented, however, a slight preferential direction in the <001> direction parallel to the x and y axes is visible (red grains in Figures 18 and 19). This is also confirmed in Figure 20. The grain boundaries were divided into low-angle (5–15°) and high-angle (above 15°). In the selected area of the sample, 1.85% of low-angle and 98.15% of high-angle grain boundaries are found (see Figure 21). For a more detailed description of the grain boundaries, special grain boundaries were also examined on the sample, where twins are included (see Figure 21). Twinning in the fcc structure occurs in the <111> direction.

Twins are shown in red in Figure 16 and reach 61.1% of all grain boundaries found in the structure. A GND Density map was also created in combination with the grain boundary map (see Figure 22) to investigate the dislocation concentration. The dislocation density in a selected area of the sample after hot-rolling ranges from values close to zero (areas marked in dark blue in Figure 22) to values of approximately $2 \cdot 10^{14}/m^2$ (light green). In most grains, the dislocation density is almost zero, only in selected grains (parts of grains with green area) is the dislocation density higher. The average grain size is 25.8 µm (see Figure 23).

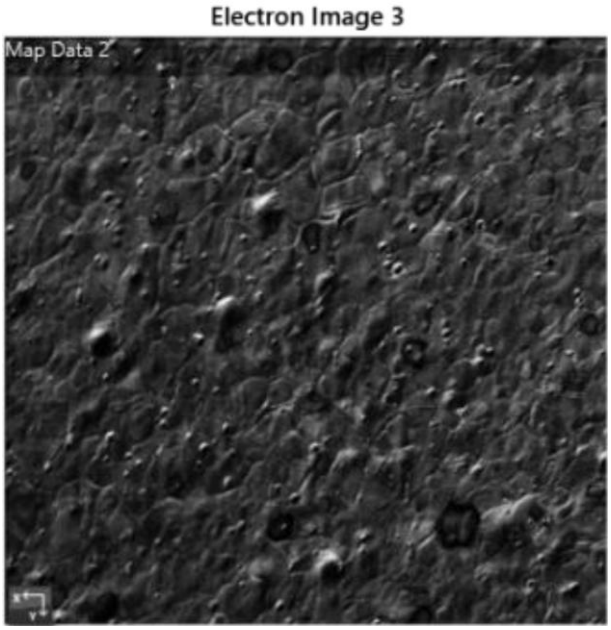

Fig. 16 *Sample area selected for EBSD analysis (sample after hot-rolling)*

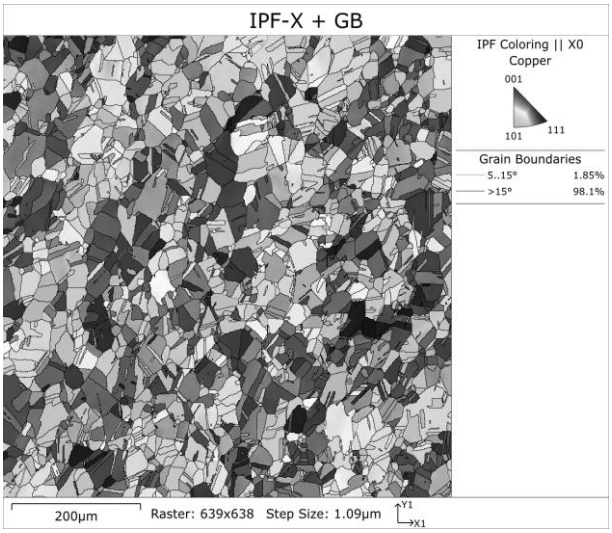

Fig. 17 *Inverse pole figure map, axis x (sample after hot-rolling)*

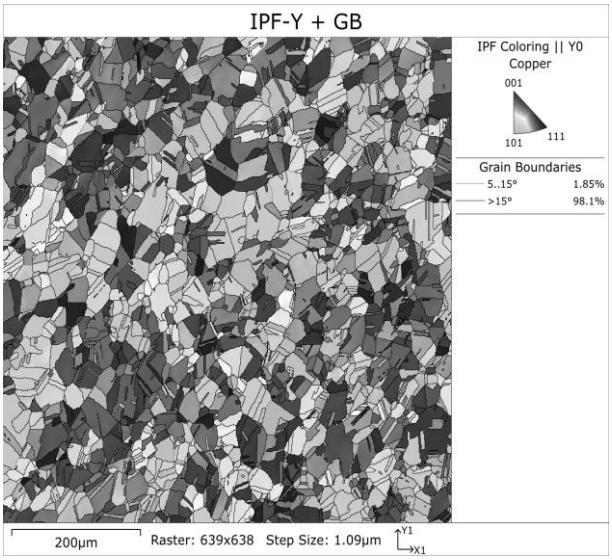

Fig. 18 *Inverse pole figure map, axis y (sample after hot-rolling)*

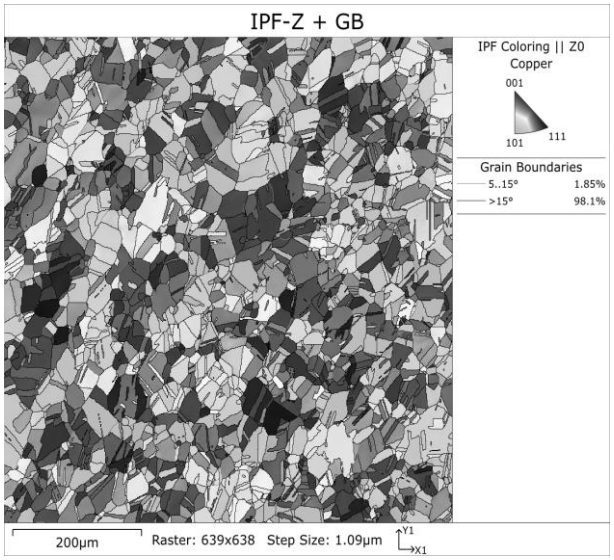

Fig. 19 *Inverse pole figure map, axis z (sample after hot-rolling)*

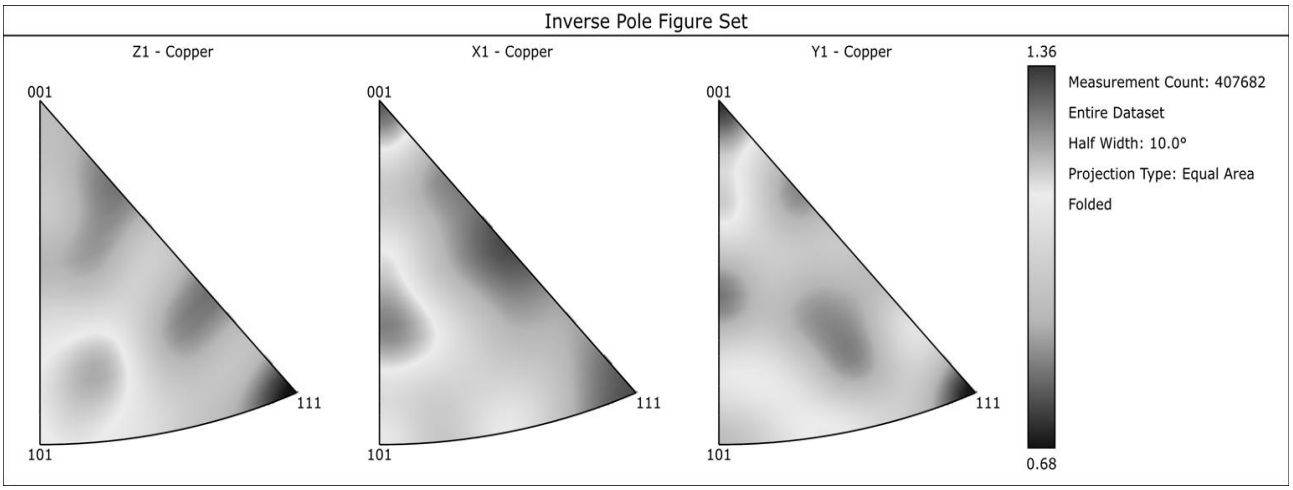

Fig. 20 *Inverse pole images for all three axes for the sample after hot-rolling*

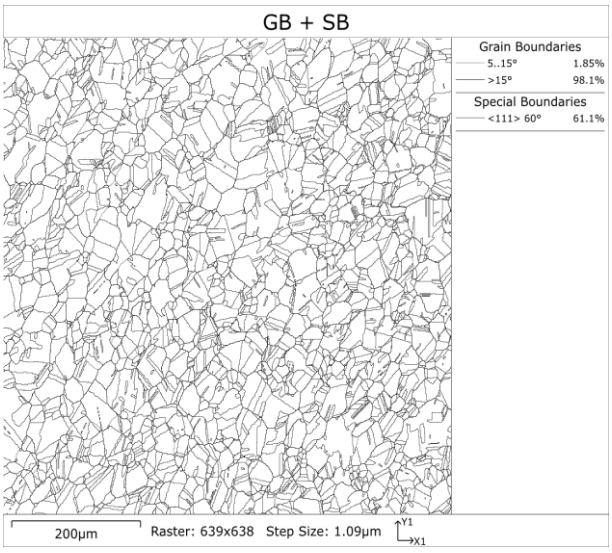

Fig. 21 *Grain boundaries including twinning in the sample after hot-rolling*

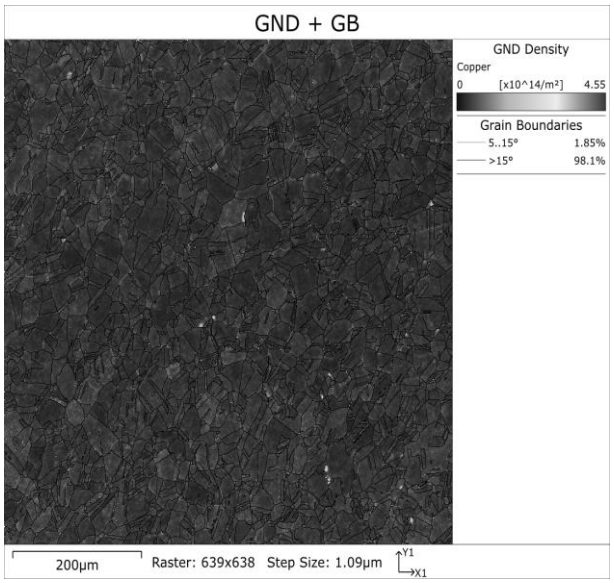

Fig. 22 *GND density of the sample after hot-rolling*

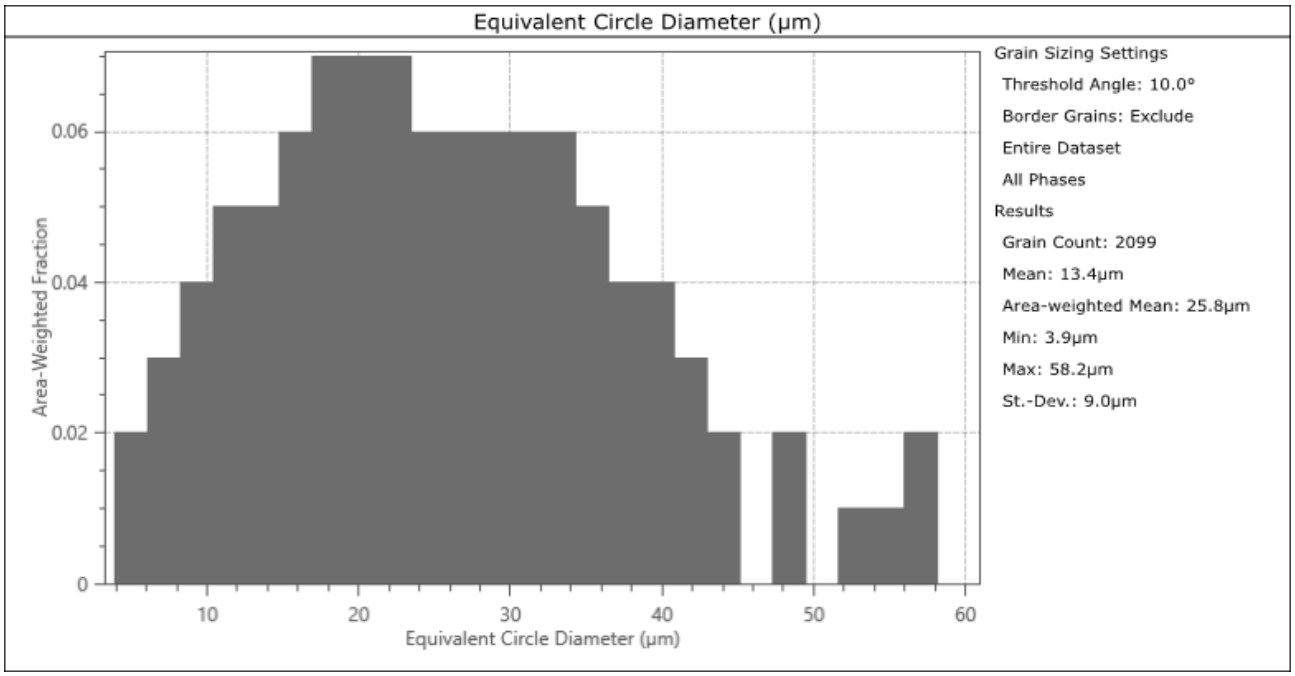

Fig. 23 *Grain size of the sample after hot-rolling*

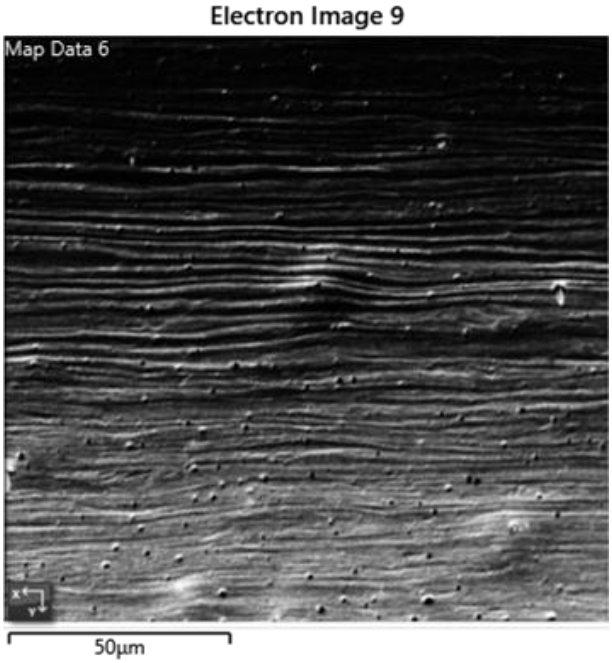

Fig. 24 *Sample area selected for EBSD analysis (sample after cold-rolling)*

Figure 24 shows sample after cold-rolling with the area selected for EBSD analysis. Figures 25, 26 and 27 show the inverse pole figure maps in the direction of each axis for sample after cold-rolling. The individual grains are elongated in the rolling direction. The black areas in these figures indicate that the samples are heavily deformed and textured, and in the areas where the microscope does not pick up the signal (black area), the copper lattice has been severely deformed and no longer picks up the signal according to the copper parameters given in Table 2. However, a preferential direction is seen in the <111> direction parallel to the x-axis and <101> parallel to the y-axis (the dark blue grains in Figure 24 and the light green in Figure 26 predominate).

This is confirmed by Figure 28. Due to the texture and deformed structure, the exact values of grain boundaries and twinning cannot be determined. A GND Density map was also created in combination with the grain boundary map (see Figure 28) to investigate the dislocation concentration. The dislocation density in the selected area is significantly higher than in the Casting and Hot Rolling sample and in most grains is around $7 \cdot 10^{14}/m^2$. In some areas, the dislocation density is even above $11 \cdot 10^{14}/m^2$. The average grain size cannot be determined in this case.

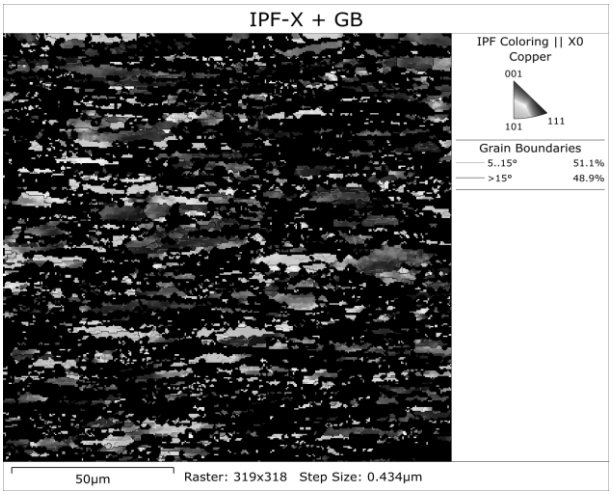

Fig. 25 *Inverse pole figure map, axis x (sample after cold-rolling)*

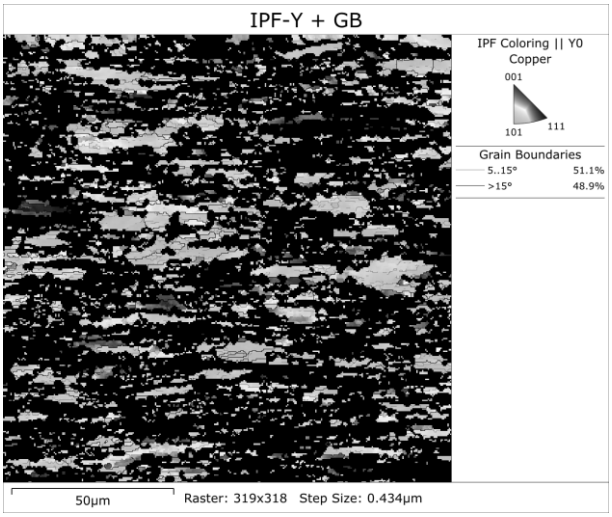

Fig. 26 *Inverse pole figure map, axis y (sample after cold-rolling)*

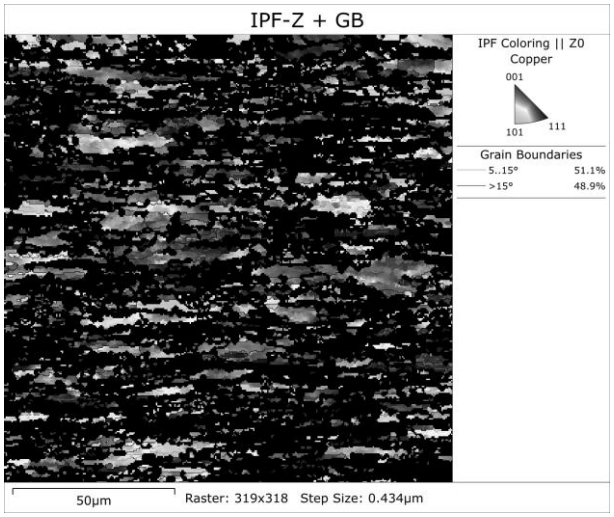

Fig. 27 *Inverse pole figure map, axis z (sample after cold-rolling)*

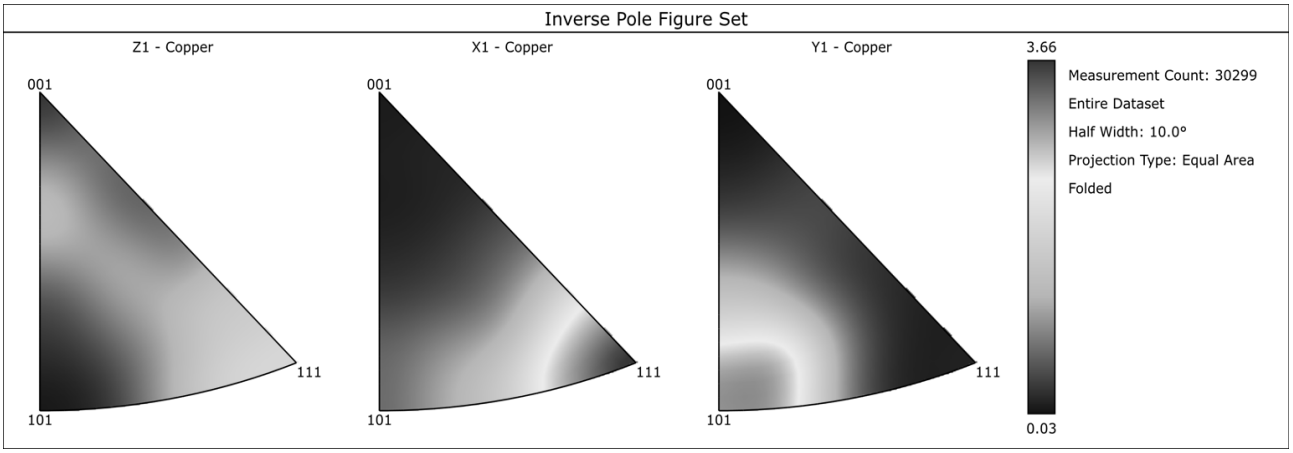

Fig. 28 *Inverse pole images for all three axes for the sample after cold-rolling*

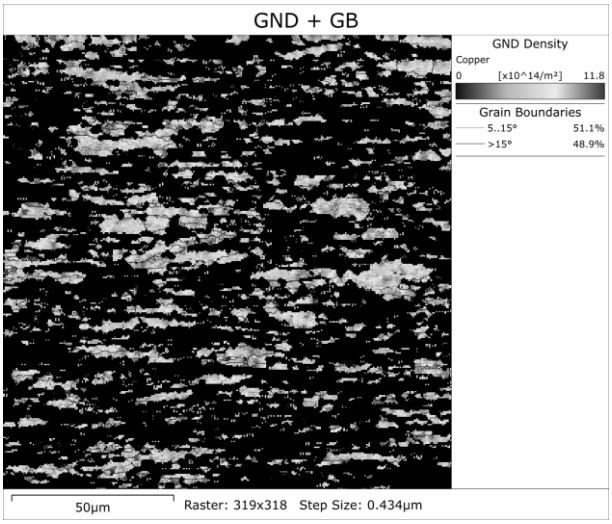

Fig. 29 *GND density of the sample after cold-rolling*

Figure 30 shows the sample after cold-rolling + annealing with the area selected for EBSD analysis. Figures 31, 32 and 33 show the inverse pole figure maps in the direction of the individual axes for the sample after cold-rolling + annealing. The individual grains are randomly oriented and a slight preferential direction in the <001> direction parallel to the z axis is visible (the red grains in Figure 33 predominate). This is also confirmed in Figure 34. The grain boundaries were divided into low-angle (5–15°) and high-angle (above 15°). In the selected area of the sample, 2.46% of low-angle and 97.54% of high-angle grain boundaries are found (see Figure 35). For a more detailed description of the grain boundaries, special grain boundaries were also examined on the sample, where twins are included. Twinning in the fcc structure occurs in the <111> direction. Twins are shown in red in the figure and account for 55.8% of all grain boundaries in the structure. A GND Density map was also created in combination with the grain boundary map (see Fig. 36) to investigate the dislocation concentration. The dislocation density in the selected area of the sample after cold-rolling + annealing is zero in most grains, reaching a value of approximately $2 \cdot 10^{14}/m^2$ in the light green areas. The average grain size is 18.1 µm, see Fig. 37.

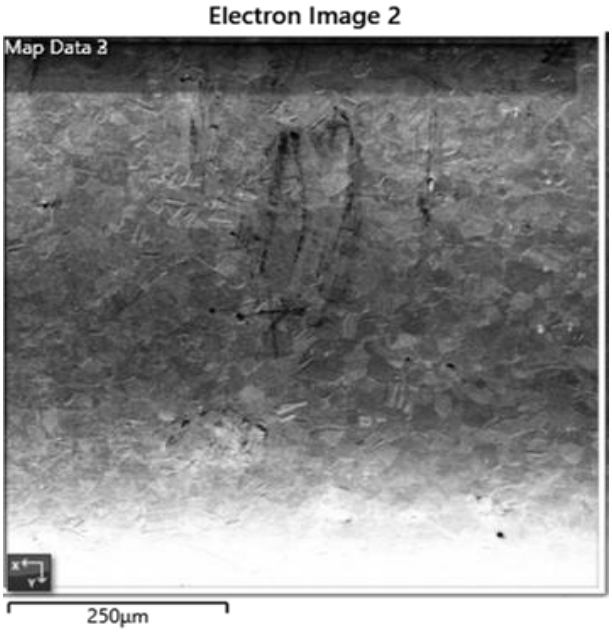

Fig. 30 *Sample area selected for EBSD analysis (sample after cold-rolling + annealing)*

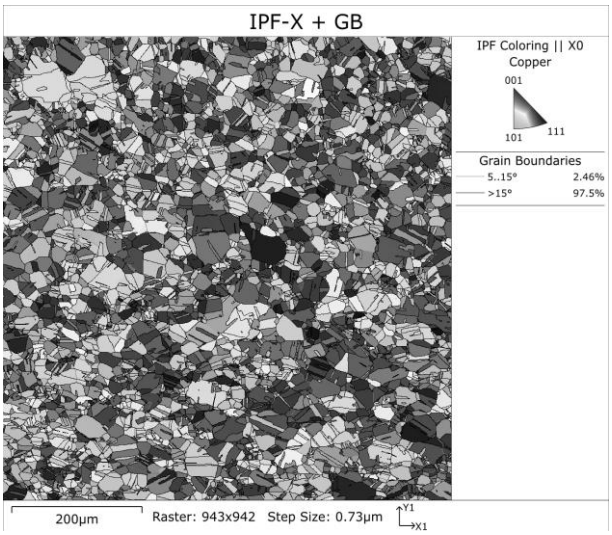

Fig. 31 *Inverse pole figure map, axis x (sample after cold-rolling + annealing)*

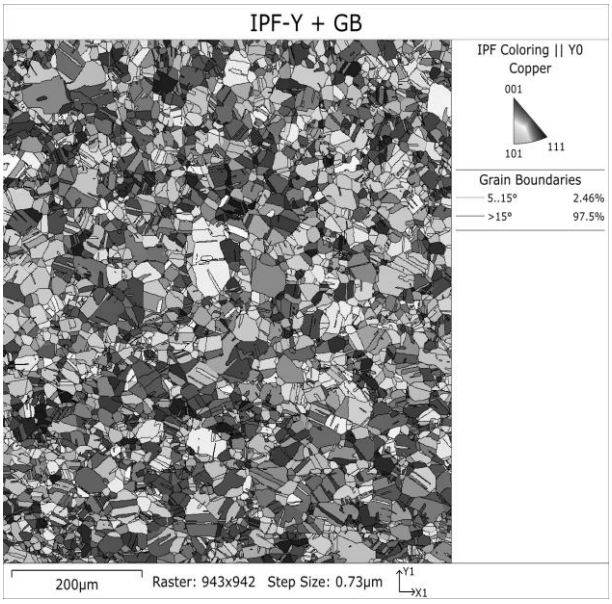

Fig. 32 *Inverse pole figure map, axis y (sample after cold-rolling + annealing)*

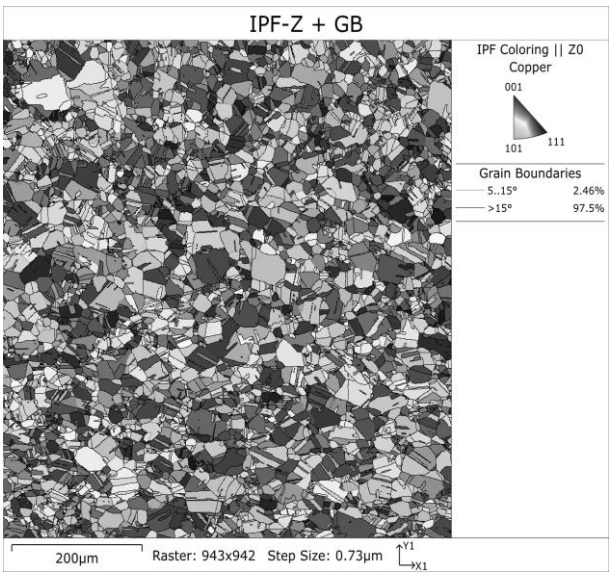

Fig. 33 *Inverse pole figure map, axis z (sample after cold-rolling + annealing)*

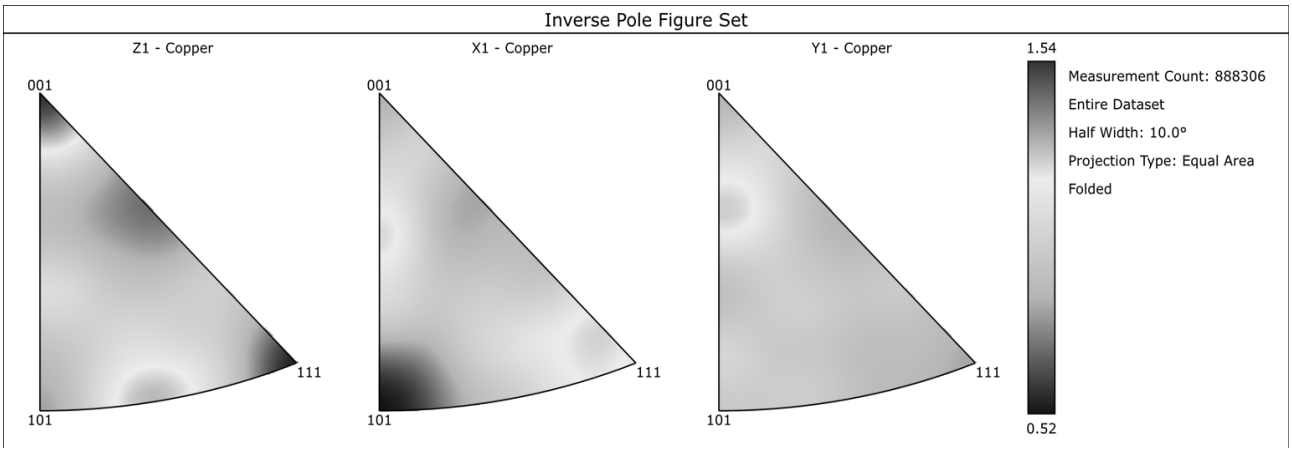

Fig. 34 *Inverse pole images for all three axes for the sample after cold-rolling + annealing*

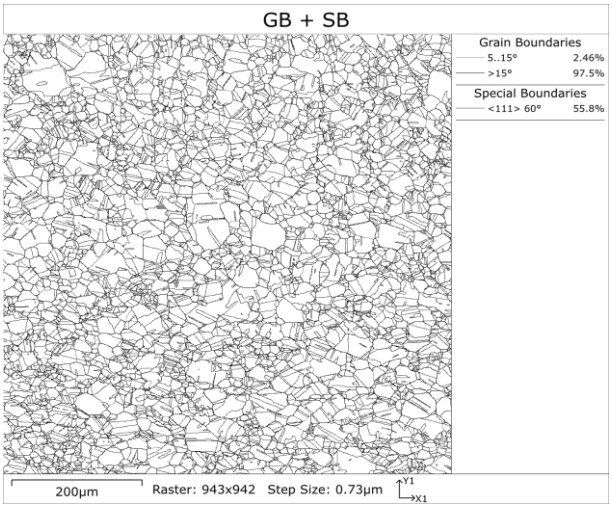

Fig. 35 *Grain boundaries including twinning in the sample after cold-rolling + annealing*

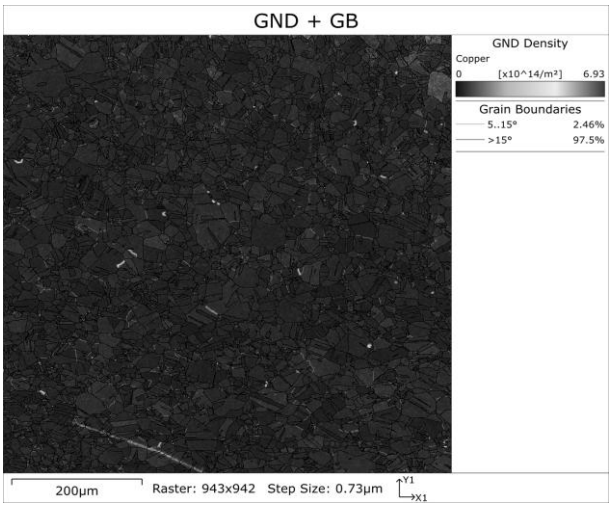

Fig. 36 *GND density of the sample after cold-rolling + annealing*

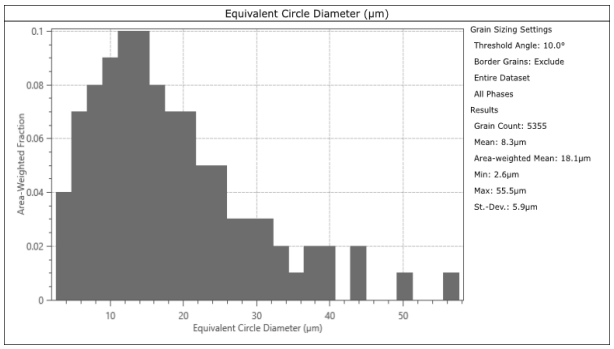

Fig. 37 *Grain size of the sample after cold-rolling + annealing*

3.3 Hardness of the samples

For the hardness test of CuZn10 alloy, the Vickers microhardness test was chosen, which uses a diamond pyramid with an apex angle of 136 degrees as an indenter. For this type of material, a load of 0.1 kg (100 g) and an indenter time of 10 seconds were chosen as input parameters. The microhardness was examined on samples with various technological treatments, which included casting, hot rolling, first cold rolling, second cold rolling and annealing. On each of these samples, 10 measurements were made at different locations of the sample so that the results were as objective as possible. This microhardness measurement was performed on a Shimadzu HMV-2 hardness tester.

The arithmetic mean and standard deviation of the determined microhardness values were subsequently calculated. The microhardness for casting reaches 63.35 HV 0.1, for hot-rolling 60.24 HV 0.1, for cold-rolling 162.3 HV 0.1, and for annealing 80.87 HV 0.1. Individual measurements including arithmetic mean and standard deviations are shown in Table 3.

Tab. 3 *Vickers microhardness measurement values*

	Casting	Hot-rolling	Cold-rolling	Cold-rolling + annealing
	61.9	58.9	164	85.7
	63.9	56.6	156	84.2
	66.3	58.9	160	89.5
	62.9	57.1	162	87.2
	67.0	62.9	161	77.5
	64.2	62.9	168	75.7
	63.9	66.3	161	74.9
	62.3	60.1	157	75.7
	61.9	60.4	169	81.2
	59.2	58.3	165	77.1
Average hardness	63.35	60.24	162.30	80.87
Standard deviation	2.26	3.01	4.27	5.41

When examining a sample that has been processed by hot-rolling above the recrystallization temperature, the resistance to deformation decreases, grain boundaries disappear and new grains are formed. Furthermore, the ductility increases, toughness and internal stress in the material decrease. Thus, the microhardness decreases, as can be seen in the measured values in Tab. 3.

The microhardness values of the samples after the cold-rolling show a sharp increase, which is caused by plastic deformation in the cold, for which higher microhardness is typical because the grains elongate in the direction of plastic deformation and the internal stress also increases here, which leads to strengthening.

In the annealed sample (500 °C for 1 hour), the microhardness decreased by about half, which may also be caused by a slight change in the crystal structure, and mainly due to the release of internal stresses in the material under investigation in our case CuZn10.

4 Conclusion

The results showed that the processing technology has a significant effect on the microhardness of the alloy. The highest microhardness values were recorded for samples that underwent the cold-rolling process, while the lowest values were recorded for samples that underwent the casting and hot-rolling process.

Microstructure analysis showed that the processing technology also affects the size and orientation of the grains. The cast samples without subsequent treatment showed large grains. During hot-rolling, the grain size had already decreased. Subsequent cold-rolling caused the grains to stretch in the rolling direction and significantly strengthened the grains and formed a deformation structure (there were significantly more dislocations in the samples). After annealing the cold rolled samples, there was a significant reduction in the grains and the removal of stress in the material, as well as the removal of dislocations.

Acknowledgement

Supported by the OPST Project Green Energy Technologies Centre of UJEP., Reg. No CZ.10.02.01/00/24_061/0000462

Spolufinancováno Evropskou unií

STÁTNÍ FOND ŽIVOTNÍHO PROSTŘEDÍ ČESKÉ REPUBLIKY

Ministerstvo životního prostředí

References

[1] A.I. TOULFATZIS, G.A. PANTAZOPOULOS, C.N. DAVID, D.S. SAGRIS, A.S. PAIPETIS, Machinability of Eco-Friendly Lead-Free Brass Alloys: Cutting-Force and Surface-Roughness Optimization, *Metals* 8(4) (2018) 250.

[2] V. WEISS, J.J.M.T. SVOBODOVÁ, The use of colour metallography and EDS for identification of chemical heterogeneity of selected aluminium alloys copper and zinc alloyed, *Manufacturing Technology* 15(6) (2015) 1048-1053.

[3] D. POROŚ, H.J.M.T.J. SKOWRONEK, Technological Considerations in WEDM of Carbon Fiber Reinforced Silicon Carbide Composites (Cf-SiC), 24(6) (2024) 940-951.

[4] W. WOŁCZYŃSKI, Z. LIPNICKI, A. BYDAŁEK, A.J.A.O.F.E. IVANOVA, Structural zones in large static ingot. forecasts for continuously cast brass ingot, *Archives Of Foundry Engineering* 16(3) (2016) 141-146.

[5] W. WOŁCZYŃSKI, A.A. IVANOWA, P.J.Z.N.A.M.W.S. KWAPISIŃSKI, Mathematical predictions of brass/steel ingot structures, *Scientific Journals of the Maritime University of Szczecin* (56 (128) (2018) 47-54.

[6] Ü.S. SAKALLI, Ö.F. BAYKOÇ, B. BIRGÖREn, Stochastic optimization for blending problem in brass casting industry, *Annals of Operations Research* 186(1) (2011) 141-157.

[7] Q. ZHAO, Z. LIU, S. LI, T. HUANG, P. XIA, L. LU, Evolution of the Brass texture in an Al-Cu-Mg alloy during hot rolling, *Journal of Alloys and Compounds* 691 (2017) 786-799.

[8] F. QAYYUM, M. SHAH, S. MANZOOR, M. ABBAS, Comparison of thermomechanical stresses produced in work rolls during hot and cold rolling of Cartridge Brass 1101, *Sage Journals* 31(3) (2015) 317-324.

[9] M. HATHERLY, A.S. MALIN, C.M. CARMICHAEL, F.J. HUMPHREYS, J. HIRSCH, Deformation processes in hot worked copper and α brass, *Acta Metallurgica* 34(11) (1986) 2247-2257.

[10] F.H. KAVARANA, K.S. RAVICHANDRAN, S.S. SAHAY, Nanoscale steel-brass multilayer laminates made by cold rolling: microstructure and tensile properties, *Scripta Materialia* 42(10) (2000) 947-954.

[11] A.A. SALEH, C. HAASE, E.V. PERELOMA, D.A. MOLODOV, A.A. GAZDER, On the evolution and modelling of brass-type texture in cold-rolled twinning-induced plasticity steel, *Acta Materialia* 70 (2014) 259-271.

[12] S. KUSMIERCZAK, N. NAPRSTKOVA, M. KUBA, Analysis of the Defects Causes in Rolled Brass Sheet, *Manufacturing Technology* 14(3) (2014) 347-351.

[13] S.O. YILMAZ, T. TEKER, Y.O. BATMAZ, Ç. YÜKSEL, Effect of thermomechanical processing on the mechanical properties of CuZn10 alloy, *De Gruyter Bill* 64(7) (2022) 1026-1032.

[14] A. BAGHERI, A. SHABANI, M.R. TOROGHINEJAD, A. TAHERIZADEH, Post-rolling annealing of a multilayered Brass/IFS/Brass composite: An evaluation of anisotropy, formability, and mechanical properties, *Journal of Materials Research and Technology* 19 (2022) 732-746.

[15] T. KONKOVA, S. MIRONOV, A. KORZNIKOV, G. KORZNIKOVA, M.M. MYSHLYAEV, S.L. SEMIATIN, Annealing behavior of cryogenically-rolled Cu–30Zn brass, *Journal of Alloys and Compounds* 648 (2015) 858-863.

[16] W. WANG, B. WANG, H.J.M.T.J. ZHANG, Research on Gradient Temperature Rolling Process and Deformation Uniformity of 10Ni5CrMoV Heavy Plate, 25(2) (2025) 265-272.

[17] Y.L. SHABTAY, M. AINALI, A. LEA, New brazing processes using anneal-resistant copper and brass alloys, *Materials & Design* 25(1) (2004) 83-89.

[18] E. PATERSON, J.W. BOND, A. ROBERT HILLMAN, A Comparison of Cleaning Regimes for the Effective Removal of Fingerprint Deposits from Brass, *Journal of Forensic Sciences* 55(1) (2010) 221-224.

[19] A. ATRIAN, F. FERESHTEH-SANIEE, Deep drawing process of steel/brass laminated sheets, *Composites Part B: Engineering* 47 (2013) 75-81.

[20] R. DWIVEDI, G. AGNIHOTRI, Numerical Simulation of Aluminum and Brass Material Cups in Deep Drawing Process, Materials Today: *Proceedings* 2(4) (2015) 1942-1950.

[21] J. LUSTINEC, M. ROSKO, V. OCENASEK, Structural and Mechanical Properties of CuZn30 Cartridge Brass in Real Production Conditions, *Manufacturing Technology* 23(6) (2023) 846-852.